
ATCN: RESOURCE-EFFICIENT PROCESSING OF TIME SERIES ON EDGE

A PREPRINT

Mohammadreza Baharani
 The UNC at Charlotte
 Charlotte, NC
 mbaharan@uncc.edu

Hamed Tabkhi
 The UNC at Charlotte
 Charlotte, NC
 htabkhiv@uncc.edu

August 3, 2021

ABSTRACT

This paper presents a scalable deep learning model called Agile Temporal Convolutional Network (ATCN) for high-accurate fast classification and time series prediction in resource-constrained embedded systems. ATCN is a family of compact networks with formalized hyperparameters that enable application-specific adjustments to be made to the model architecture. It is primarily designed for embedded edge devices with very limited performance and memory, such as wearable biomedical devices and real-time reliability monitoring systems. ATCN makes fundamental improvements over the mainstream temporal convolutional neural networks, including residual connections as time attention machines to increase the network depth and accuracy and the incorporation of separable depth-wise convolution to reduce the computational complexity of the model. As part of the present work, three ATCN families, namely T0, T1, and T2, are also presented and evaluated on different ranges of embedded processors - Cortex-M7 and Cortex-A57 processor. An evaluation of the ATCN models against the best-in-class InceptionTime shows that ATCN improves both accuracy and execution time on a broad range of embedded and cyber-physical applications with demand for real-time processing on the embedded edge. At the same time, in contrast to existing solutions, ATCN is the first deep learning-based approach that can be run on embedded microcontrollers (Cortex-M7) with limited computational performance and memory capacity while delivering state-of-the-art accuracy.

1 Introduction

The astonishing growth in deep learning algorithms has changed how embedded and cyber-physical systems (CPS) process the surrounding environment and has significantly improved the overall CPS performance on delivering their assigned tasks. For instance, the deep learning algorithms and architectures have powered the embedded systems in visual sensing applications such as pedestrian and object tracking [1, 2], action detection [3, 4]. Another dimension of deep learning, which has recently emerged in the edge, is time series analysis and forecasting. Healthcare [5, 6, 7], device health monitoring [8, 9, 10], machine translation [11, 12] are some examples of deep learning use in time sequence analysis.

For most deep learning practitioners, recurrent networks and especially two elaborated models, namely, LSTM [13] and GRU [14], are synonymous with time series analysis due to its notable success in sequence modeling problems such as machine translation, language processing, and device health monitoring. These models interpolate the output based on the current and temporal information, which is learned and captured in the hidden states and propagated through the time from one cell to the next adjacent cell. The propagation chain of hidden state causes two significant issues [15]: 1) gradient instability such as vanishing/exploiting gradients and 2) fewer levels of parallelization due to existing dependencies across the cells.

Temporal Convolutional Networks (TCN) was first proposed based on an adaptation of WaveNet [16] and Time-Delay Neural Network [17]. It orchestrates dilated convolutions in Encoder-Decoder architecture to have a unified framework for action segmentation. Later, Bai et al. [18] designed a Generic TCN (GTCN) architecture for sequence modeling,

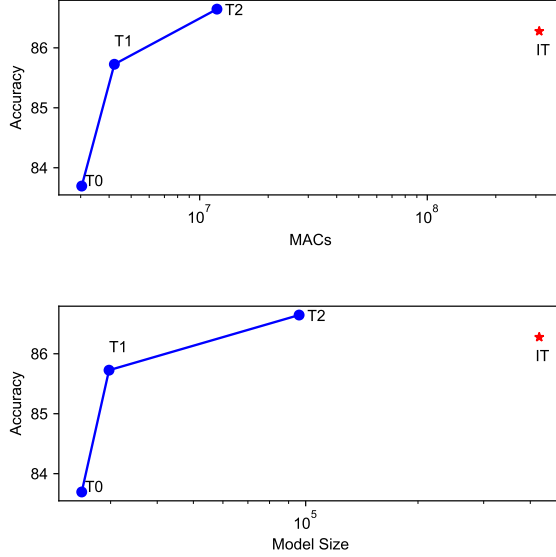


Figure 1: Model complexity comparison of three different ATCN families against InceptionTime (IT)

which outperforms LSTM on time-series and sequence modeling tasks. However, the GTCN suffers from two main drawbacks: 1) the size of dilation increases exponentially by the layer, which prevents the designer from increasing the depth of the network, 2) it uses two standard convolutions per each layer, which is computationally expensive for resource-constrained embedded systems. InceptionTime (IT) [19] is another off-the-shelf CNN to classify time series based on CNN, representing a scalable, accurate solution; however, execution on a microcontroller is entirely out of reach of InceptionTime.

This chapter proposes a novel extension of TCN called ATCN for light-weight processing of time series on embedded and edge devices. We introduced Spectral-Temporal Convolution Block (STCB) to decrease the number of MAC operations and the model size of TCN to make it applicable for embedded devices while maintaining a comparable or better accuracy over IT. Various configurations of these three blocks can be combined to form different ATCN families that can each meet various design constraints. FIG. 1 illustrates the capacities and scalability of three different ATCN families on accuracy and model complexity trade-off over 70 benchmarks from the UCR 2018 dataset [20] against IT. The T0 configuration reduces the MACs and model size by $102.38\times$ and $16.84\times$ over IT, respectively. T1 performance is 4.03% better than T0 and has a $73.59\times$ reduction in MACs, and a $14.23\times$ reduction in model size over IT. Both T0 and T1 can be executed on an ARM Cortex-M7 microcontroller explained in the experimental section in detail. As a final improvement, T3 reduces the MACs and model size for $26.07\times$ and $4.4\times$ over IT while increasing accuracy by 0.37%.

Overall, the key contributions of this chapter are:

- Proposing ATCN, which achieves higher or comparable accuracy over state-of-the-art models with significantly lower computation complexity for embedded devices.
- Creating a network template supported by automated design flow for scalable generation and training different configurations of ATCN concerning the complexity of problem and latency requirements.

The rest of this article is organized as the following: Section 2 briefly discusses the use of time-series analysis in embedded and CPS. Section 3 provides background on generic TCN and its architecture. In section 4, we elaborate on the Temporal-Spectral block, the ATCN architecture, and its hyperparameters. Section 5 presents the experimental results including comparison with existing approaches, and finally Section 6 concludes this article.

2 Related Works

Traditional convolutional neural networks are used in computer vision applications due to their success in capturing the spatial features within a two-dimensional frame. Recently, research has shown that specialized CNNs can recognize patterns in data history to predict future observations. This gives researchers interested in time-series forecasting options to choose from over RNNs, which have been regarded in the community as the established DNN for time-series predictions. In one such case, Dilated Convolutions (DC) have been shown to achieve state-of-the-art accuracy

in sequence tasks. In the first use of DC, WaveNet [21] was designed to synthesize raw audio waveform, and it outperforms the LSTM. Later, Lea et al. [22] proposed TCN, a unified network based on WaveNet DC, for video-based action segmentation. In the same trend, the gated DC was used for the sequence to sequence learning [23]. The proposed approach beats deep LSTM in both execution time and accuracy.

GTCN [15] is a generic architecture designed for sequence modeling. The design of GTCN was based on two main principles: 1) there shouldn't be any information leakage from future to past, 2) the network should be able to receive any arbitrary input length similar to RNN. Since the main fundamental component of GTCN is based on variable-length DC, it brought higher parallelization and flexible receptive field in comparison to RNN. Also, since the gradient flow of GTCN is different from the temporal path of RNN, it is more resistant to the problem of gradient instability. Recent researches have taken advantage of GTCN benefits or similar architectures in their works. In the work of [24], a modified version of GTCN with depth-wise convolution has been used to enhance the speech in time-domain. The DeepGLO [25] is another work that used a global matrix factorization model regularized by a TCN to find global and local temporal in high dimensional time series.

InceptionTime is an ensemble of CNN blocks called Inception Module and proposed as a solution for the Time Series Classification (TSC) problem. The network architecture was constructed based on the Inception-v4 [26] structure, and it employed a larger kernel size to beat enormous and complex models such as the HIVE-COTE [27]. Nonetheless, it is still exceedingly heavy for the microcontroller with limited resources, such as ARM Cortex-M series, or even legacy embedded ARM Cortex-A series CPUs.

The chapter proposes ATCN for embedded and resource-constrained hardware to address time-series domain problems, which is on par with InceptionTime in terms of accuracy performance. We have put our claim on test in Section 5 by comparing ATCN against InceptionTime over 70 benchmarks from UCR time-series datasets. Additionally, we have reported the execution profile of the Cortex-M7 and Cortex-A57 when running ATCN families. We have shown that ATCN improves or maintains the overall system accuracy for these three cases while minimizing computational complexity and model size. In the next section, we study the structure of DC in-depth to prepare the ground for introducing ATCN in Section 4.

3 Background: Temporal Neural Networks

GTCNs are designed around two basic principles: 1) the convolutional operations are causal, i.e., predictions are made based only on current and past information; 2) the network receives an input sequence of arbitrary length and maps it to an output sequence of the same length [15]. Based on principle number 2, in order to map the final output to an arbitrary size, the output of the last DC output can be connected to a linear layer. This adds flexibility by allowing a final output length to be independent of the input length. The naive causal convolutions, which have a dilation rate of 1, are inherently inefficient as their sequence history scales with size linear to the depth of the network.

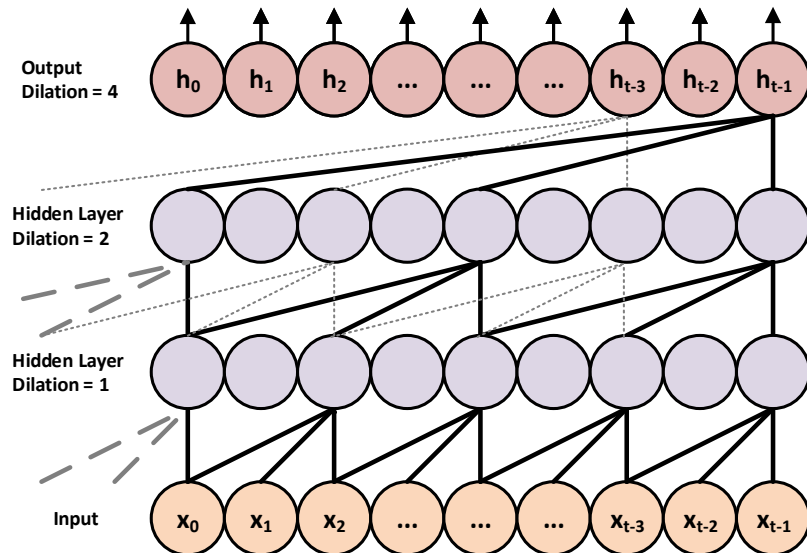


Figure 2: Dilated Causal Convolution.

The solution here incorporates dilated convolutions to exponentially scale the receptive field, as shown in Fig. 2. The first convolution with dilation rate $d=1$ maps the input vector $X = [x_1, x_2, \dots, x_{t-1}]$ to the higher dimension. Then, GTCN increases the d for the next convulsions exponentially to increase the receptive field. The minimum output sequence length, before mapping to the linear layer, can be determined by calculating its receptive field: [28]:

$$rf = 1 + \sum_{l=1}^L [k(l) - 1] \times d(l), \quad (1)$$

where $l \in \{1, 2, 3, \dots, L\}$ is the layers, k is the kernel size, and $d(l)$ is the dilation rate at layer l . This means that as the depth of the network increase, so does the receptive field. The dilated convolution of F on element s of a sequence X is given as:

$$F(s) = (X *_d f)(s) = \sum_{i=0}^{k-1} f(i) \cdot x_{s-d \cdot i}, \quad (2)$$

where $X \in \mathbf{R}^n$ is a 1-D input sequence, $*_d$ is dilated convolution operator, $f : \{0, \dots, k-1\} \in \mathbf{R}$ is a kernel of size k and d is the dilation rate [15, 28]. For applications requiring a very large rf , it is also essential to provide stability in the later layers subject to the vanishing gradient problem. A popular technique in traditional CNN architectures, the residual block [29], provides a “highway” free of any gated functions, allowing information to flow from the early layers to the last layers unhindered.

These connections can be seen in the final GTCN architecture shown in Fig. 3. The GTCN consists of L hidden layer and an optional linear layer to map the input size i to arbitrary output size. Each hidden layer has two regular dilated convolution and two ReLU activation function. There can also be an upsampling unit, such as point-wise convolution, in the first hidden layer of GTCN to map 1-D input sequence to a higher dimension to guarantee the element-wise addition receives tensor of the same dimension.

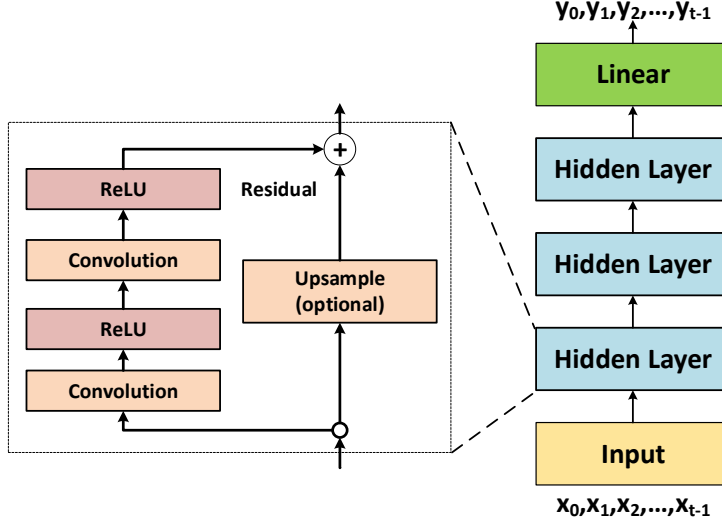


Figure 3: Structure of Generic TCN.

The design of GTCN suffers from two problems: 1) exponential growth of dilation size, 2) the existence of two regular convolutions per layer. The exponential growth of dilation size and requirement of having the same length for both input and output of dilated convolution force the network designers to have excessive padding at the higher layers. Also, the implementation of two convolutions blocks per layer makes the GTCN costly for CPS. In the next section, we address the problems mentioned above by introducing ATCN architecture.

4 ATCN: Agile Temporal Convolutional Networks

In this section, we introduce the architecture of ATCN. At first, we discuss the essential components, and then we elaborate on the hyper-parameters, and in the end, we present the ATCN architecture and its model builder.

4.1 Network Structure

The ATCN architecture can be created by chaining STCBs and altering their configurations. Each STCB is composed of a pointwise (expansion), a group, and a pointwise (projection) convolution. We visualized the STCB in Fig. 4(a). The Max Pooling layers are optional. It lets architects downsample temporal information to minimize computational complexity while embedding that information in higher or lower dimensions. The extreme case of STCB is when the group size and its input channel size are equal. In this case, the group-convolution is set to a depthwise, and the ATCN network synthesizer will remove the maximum pooling and add a skip-line between element-wise addition and the STCB input. The final architecture of ATCN is shown in 4(c). The ATCN is a mirrored residual dilated convolutional neural network. It starts with mapping the n -dimension input, which is generally 1D for the time series, to higher dimension at first layer. Then it encodes the data to lower dimension. At encoder parts, the data will be decoded to higher dimension again. Based on the final application, the output of decoder can be used for regression or classification problems. In the rest, we discuss the details of STCB and the network hyper-parameters.

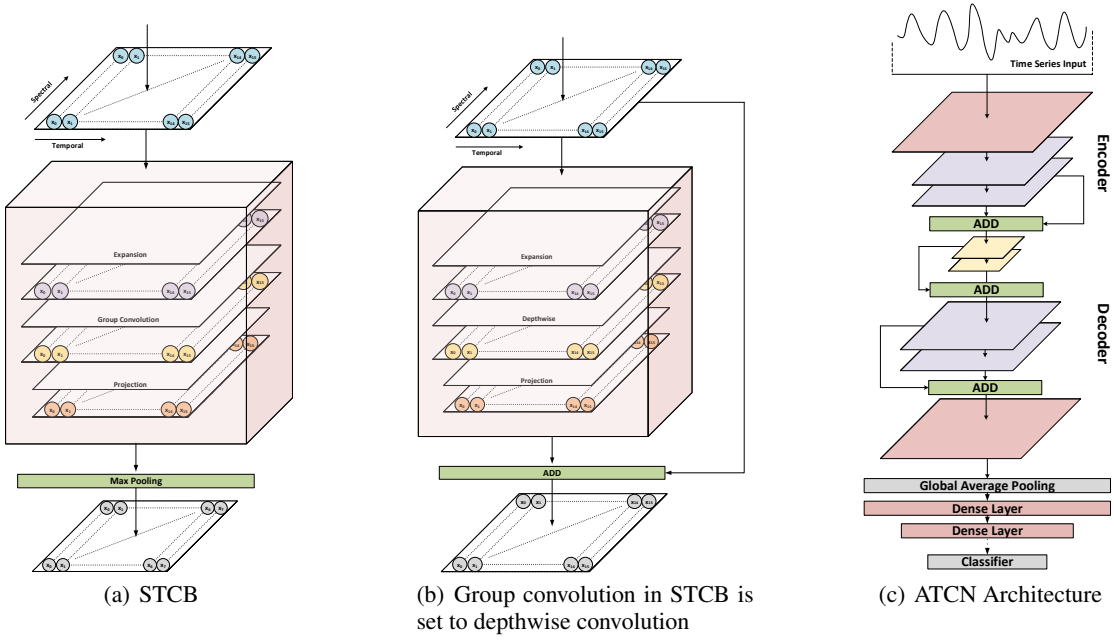


Figure 4: Structure of ATCN blocks. The non-linearity activation and batch normalization units after each convolution are not depicted.

4.1.1 ATCN Structure

The first layer of ATCN is standard convolution with an optional MaxPooling for downsampling the input. A padding unit is also added before standard convolution and expansion convolution in STCB to ensure that the input and output tensors of the block have the same size to satisfy principle number 2 of GTCN. The $2p$ zeros are added symmetrically by padding unit, where p is given by:

$$p = \lceil \frac{(o-1) \times s + (k-1) \times (d-1) - i + k}{2} \rceil, \quad (3)$$

where o is the output size, i is the input size, s is the stride, k is the kernel, and d is the dilation. After each convolution, 1D batch normalization and a non-linear activation function is also added. In this research, we used *Swish* as activation function:

$$\text{Swish}(X) = X \odot \text{Sigmoid}(X), \quad (4)$$

where \odot is Hadamrd or element-wise multiplication. Fig. 5(a) depicts the performance of different activation functions on MNIST validation loss.

The STCB consists of expansion, followed by a group and another projection convolution. The task of expansion convolution is to map input channel size, c_{in} , to higher or same dimension, c_{out}^{exp} , where $c_{out}^{exp} = \alpha \times c_{in}$, $\alpha \geq 1$.

On the contrary, pointwise projection embeds and maps the feature extracted from the group convolution to the block output size, c_{out} . For the case of depthwise convolution, we set $group$, which manages the connection between input and output, to c_{out}^{exp} . For this case, the convolution weight shape changes from (c_{out}, c_{in}, k) to $(c_{out}, 1, k)$, where k is the kernel size. We designed the network synthesizer so that if $c_{in} = c_{out}$, the skip line is automatically created from input to the elementwise addition. Then, the input will be added to the residual output from the pointwise projection. The residual connection helps the designers increase the network's depth without being worried about the vanishing gradient problem. The model synthesizer considers group convolution rather than depthwise for the case that MaxPooling is selected. The reason for doing so is based on this observation that for downsampling the input, which has an activated max-pooling unit, group convolution helps to better map temporal information to a higher dimension without drastically increasing computation complexity and the model size. The only constraint imposed by group convolution is that its output channel size, c_{out}^{gc} , should be divisible by c_{out}^{exp} . The two extreme G-CNN cases are when $group = c_{in}^{gc}$ and $group = 1$. In the former case, the group convolution is a depthwise convolution, and in the latter, it is a standard convolution. Formally, the weight shape for group convolution is $(c_{out}, \frac{c_{in}}{group}, k)$. We depict the effect of altering the $group$ values in Fig. 5(b) for MNIST digit classification. As we can see, reducing the $group$ value increases the network capacity to minimize the validation loss.

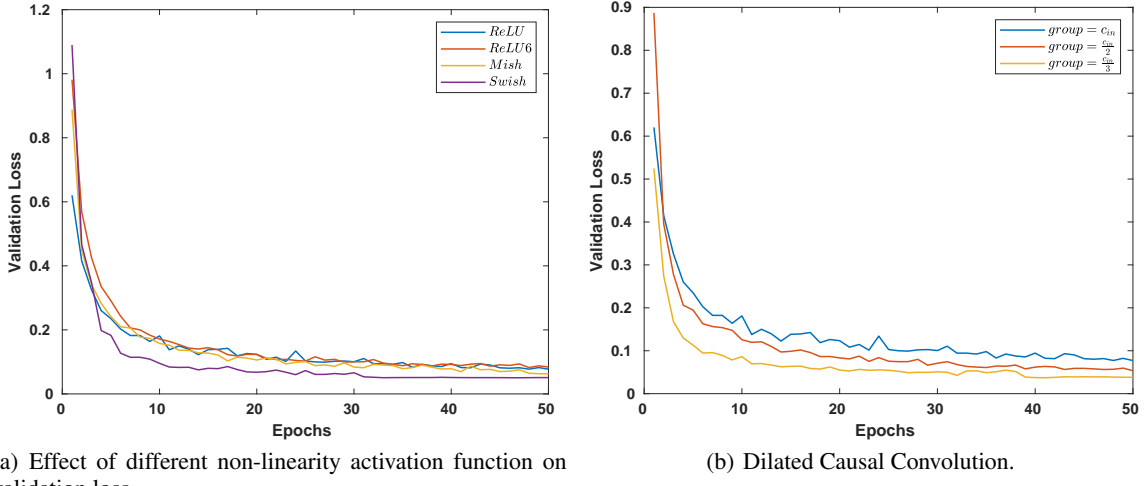


Figure 5: The effect of different non-linearity activation function, σ , and $group$ value on final validation loss.

4.2 ATCN hyper-parameters

For designing the ATCN network architecture, three knobs should be altered based on the problem complexity (sequence classification, prediction, or segmentation), the input size, the network models, and computational cost trade-off. In the rest, we fully elaborate on each of them.

4.2.1 Dilation rate

For a fixed input size, if we increase the number of layers, based on the GTCN architecture guideline, we need to increase the dilation rate exponentially. This decision will help the network have a higher receptive field; however, based on principle number 2, we need to pad the features excessively to have the same input and output size. This unnecessary padding results in 1) more computation and 2) CNN performance degradation. We observed linear growth for dilation would help the network with more than six layers to have better feature representation. Although the dilation rate can be defined as a function of layer number, we increased it after each block with activated downsampling in the experimental results. This decision helps design a deep ATCN for the cases where input size, i , is small.

4.2.2 Kernel size

It is recommended that the kernel size, k , is large enough to encompass enough feature context based on the problem complexity. However, based on Eq. 3, it is a good practice to decrease the kernel size for higher layers to ensure p is not growing exponentially. By contrast, if we increase the dilation rate, based on Eq. 1, the kernel size can be reduced

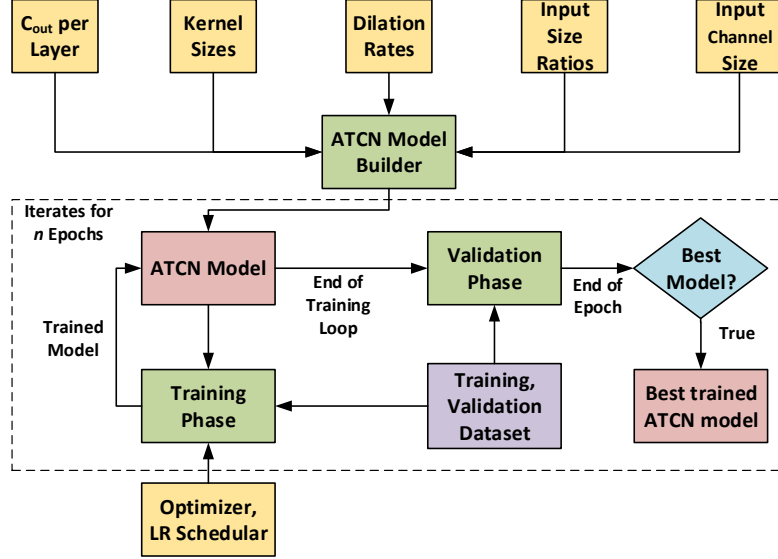


Figure 6: ATCN model synthesizer and training framework.

without concern for the receptive field. Embedded devices gain two crucial advantages from this decision: it reduces 1) the computational complexity and 2) the model size.

4.2.3 Number of layers

Similar to the dilation rate, if we need to increase the network's depth to increase its capacity, it is recommended to gradually decrease kernel size and have a linear growth for dilation. We can alter both after each block with downsampling units. This decision helps the final structure to have enough receptive field to cover feature context without increasing the MAC operations and model sizes.

4.3 ATCN Model Synthesizer

We depict the inputs of *ATCN Model Synthesizer* and the framework for its training in Fig. 6. The ATCN Model Synthesizer receives Input Channels, Kernel Sizes, Dilation Rates, Input Ratios, and finally, the first *Input Channel Size* to design the ATCN network architecture. In the rest, we explain each of the ATCN Model Synthesizer inputs in detail.

4.3.1 c_{out} per Layer

: It is a vector of size L , where L is the number of layers (blocks). The c_{out}^l defined in $\mathbf{C}_{out} = [c_{out}^1, c_{out}^2, \dots, c_{out}^L]$, decides the output channel for layer l . For this research, the values in vector \mathbf{C}_{out} are descending-ascending (Auto-Encoder architecture) to code the feature to lower dimension to extract temporal correlation and then maps to a higher dimension to represent extracted features for final stages.

4.3.2 Kernel Size

: The vector \mathbf{K} , $\mathbf{K} = [k^1, k^2, \dots, k^L] \mid k^l \in \mathbb{N}$, defines the kernel sizes for each layer. Based on the discussion of Section. 4.2.2, it is suited to decrease the k to minimize both model size and required computational complexity.

4.3.3 Dilation Rates

: The vector \mathbf{D} , where $\mathbf{D} = [d^1, d^2, \dots, d^L] \mid d^l \in \mathbb{N}$, defines the dilation rates per each layer. On the contrary to K , it is necessary to increase d to achieve a higher or same receptive field at deeper levels.

4.3.4 Input Size Ratios

: The $\mathbf{R} = [r^1, r^2, \dots, r^L] \mid 0 < r^l \leq 1$, defines the input ratios. For the value of $r^l < 1, l > 1$, the *ATCN Model Synthesizer* configures the STCB block with max-pooling unit. For the case of $l = 1, r < 1$, the max-pooling will be added after standard convolution; otherwise, the input and out of standard convolution will have the same size. For this research, the r^l can only be defined as $\frac{1}{2}$ or 1. For other ratios, the synthesizer can be modified to change the stride of max-pooling to satisfy the targeted ratio.

4.4 ATCN Families

We introduce three ATCN families by assigning values to the \mathbf{C} , \mathbf{K} , \mathbf{D} , and \mathbf{R} for UCR time series classification. Table 1 summarizes the configuration of T0, T1, and T2 as three candidates. Table 2 also compares their average FLOPS and number of model parameters of candidates and InceptionTime based on seventy benchmarks from the 2018 UCR time series classification, which are explained in detail in Section 5. We assign the output channels, C_{out} , in descending-ascending format to encode features to lower dimensions, then decode them to higher dimensions to represent them for the final dense layers and classifier. We have reduced the kernel size K due to the increased dilation rate, D . As a result, MACs and model parameters are reduced without compromising receptive field size. The T0 configuration reduces the MACs and model size by $102.38\times$ and $16.84\times$ over IT, respectively. T1 has also $73.59\times$ reduction in MACs, and a $14.23\times$ reduction in model size over IT. Finally, T2 reduces the MACs and model size for $26.07\times$ and $4.4\times$ over IT. The algorithmic accuracy of these models and training methods of these models are explained in 5.

Table 1: The configuration of three ATCN families

| Models | Configurations | | | |
|--------|----------------------------------|--------------------------|-------------------------------|--------------------------------------|
| | C_{out} | D | K | R |
| T0 | [32, 16, 16, 8, 8, 16, 16, 32] | [1, 2, 2, 4, 4, 6, 6, 8] | [32, 16, 16, 8, 8, 4, 4, 2] | $[\frac{1}{2}, 1, 1, 1, 1, 1, 1, 1]$ |
| T1 | [32, 16, 16, 8, 8, 16, 16, 32] | [1, 2, 2, 4, 4, 6, 6, 8] | [64, 32, 32, 16, 16, 8, 8, 4] | $[\frac{1}{2}, 1, 1, 1, 1, 1, 1, 1]$ |
| T2 | [64, 32, 32, 16, 16, 32, 32, 64] | [1, 2, 2, 4, 4, 6, 6, 8] | [64, 32, 32, 16, 16, 8, 8, 4] | $[\frac{1}{2}, 1, 1, 1, 1, 1, 1, 1]$ |

Table 2: FLOPS and number of parameters for T0, T1, T2, and InceptionTime

| Metric | Models | | | |
|---------|-----------|-----------|-----------|---------------|
| | T0 | T1 | T3 | InceptionTime |
| FLOPs | 2,377,840 | 3,329,008 | 9,457,376 | 240,430,566 |
| Params# | 24,816 | 29,424 | 95,456 | 422,498 |

5 Experimental Results

In this section, we demonstrate the capabilities of three different ATCN families by applying them to problems of UCR time series classification. T0 and T1 are compiled and utilized on ARM Cortex-M7 microcontroller series, and T2 is executed on ARM Cortex-A57. A report on RAM utilization, flash usage, and inference time is also provided.

5.1 Dataset

The experiments were conducted on 70 benchmarks publicly available from UCR Time Series Classification 2018, which vary in time length, number of classes, dataset type, sample size, and sample size. Table 1 summarizes the details of the benchmarks.

5.1.1 Data augmentation

For benchmarks whose training size is small, such as ECGFiveDays, we applied four types of data augmentation: jittering, magnitude warping [30], window warping [31], and scaling. In Fig. 7, each approach is shown in relation to the observed signal, X .

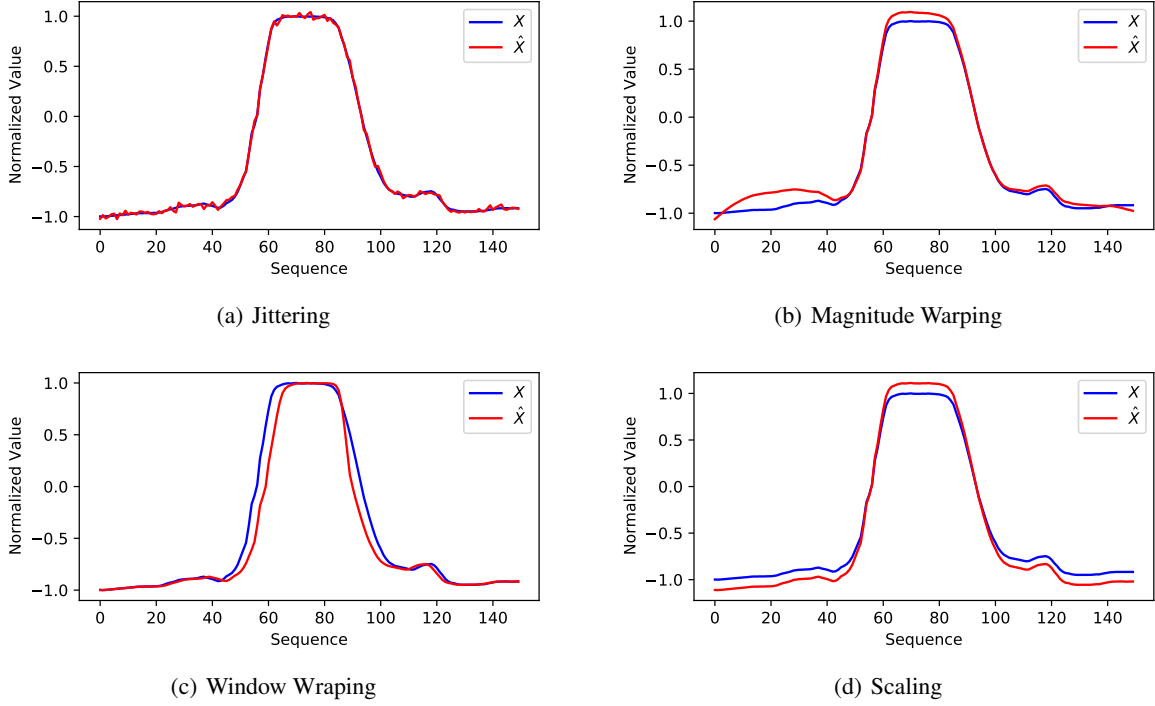


Figure 7: Different data augmentation applied on UCR dataset. X is observed signal and \hat{X} is the augmented data.

Table 3: Description of 70 benchmarks selected from UCR Time Series Classification Archive 2018

| ID | Type | Name | Train | Test | Class | Length |
|----|-----------|--------------------------|-------|------|-------|--------|
| 1 | ECG | ECGFiveDays | 23 | 861 | 2 | 136 |
| 2 | Sensor | Plane | 105 | 105 | 7 | 144 |
| 3 | Simulated | TwoPatterns | 1000 | 4000 | 4 | 128 |
| 4 | Sensor | Trace | 100 | 100 | 4 | 275 |
| 5 | Power | PowerCons | 180 | 180 | 2 | 144 |
| 6 | Spectro | Coffee | 28 | 28 | 2 | 286 |
| 7 | Simulated | BME | 30 | 150 | 3 | 128 |
| 8 | Motion | GunPointMaleVersusFemale | 135 | 316 | 2 | 150 |
| 9 | Motion | GunPointOldVersusYoung | 136 | 315 | 2 | 150 |
| 10 | EPG | InsectEPGRegularTrain | 62 | 249 | 3 | 601 |
| 11 | Sensor | Wafer | 1000 | 6164 | 2 | 152 |
| 12 | Simulated | SyntheticControl | 300 | 300 | 6 | 60 |
| 13 | Sensor | FreezerRegularTrain | 150 | 2850 | 2 | 301 |
| 14 | Traffic | Chinatown | 20 | 343 | 2 | 24 |
| 15 | Simulated | ShapeletSim | 20 | 180 | 2 | 500 |
| 16 | Motion | GunPointAgeSpan | 135 | 316 | 2 | 150 |
| 17 | ECG | TwoLeadECG | 23 | 1139 | 2 | 82 |
| 18 | Motion | GunPoint | 50 | 150 | 2 | 150 |
| 19 | Simulated | UMD | 36 | 144 | 3 | 150 |
| 20 | Sensor | DodgerLoopWeekend | 20 | 138 | 2 | 288 |
| 21 | Device | HouseTwenty | 40 | 119 | 2 | 2000 |
| 22 | Motion | ToeSegmentation2 | 36 | 130 | 2 | 343 |
| 23 | Sensor | ItalyPowerDemand | 67 | 1029 | 2 | 24 |
| 24 | Simulated | CBF | 30 | 900 | 3 | 128 |
| 25 | Image | Symbols | 25 | 995 | 6 | 398 |

Continued on next page

Table 3 – *Continued from previous page*

| ID | Type | Name | Train | Test | Class | Length |
|----|----------|--------------------------------|-------|------|-------|--------|
| 26 | Sensor | FordA | 3601 | 1320 | 2 | 500 |
| 27 | Image | Fish | 175 | 175 | 7 | 463 |
| 28 | Image | DiatomSizeReduction | 16 | 306 | 4 | 345 |
| 29 | ECG | ECG5000 | 500 | 4500 | 5 | 140 |
| 30 | ECG | ECG200 | 100 | 100 | 2 | 96 |
| 31 | Motion | ToeSegmentation1 | 40 | 228 | 2 | 277 |
| 32 | Spectro | Strawberry | 613 | 370 | 2 | 235 |
| 33 | Sensor | SonyAIBORobotSurface1 | 20 | 601 | 2 | 70 |
| 34 | Sensor | FreezerSmallITrain | 28 | 2850 | 2 | 301 |
| 35 | Image | MixedShapesRegularTrain | 500 | 2425 | 5 | 1024 |
| 36 | Sensor | DodgerLoopGame | 20 | 138 | 2 | 288 |
| 37 | Spectrum | SemgHandGenderCh2 | 300 | 600 | 2 | 1500 |
| 38 | Image | BirdChicken | 20 | 20 | 2 | 512 |
| 39 | Sensor | SonyAIBORobotSurface2 | 27 | 953 | 2 | 65 |
| 40 | Sensor | Lightning2 | 60 | 61 | 2 | 637 |
| 41 | Image | ProximalPhalanxOutlineCorrect | 600 | 291 | 2 | 80 |
| 42 | Image | ProximalPhalanxOutlineAgeGroup | 400 | 205 | 3 | 80 |
| 43 | Device | LargeKitchenAppliances | 375 | 375 | 3 | 720 |
| 44 | Sensor | Car | 60 | 60 | 4 | 577 |
| 45 | Sensor | MoteStrain | 20 | 1252 | 2 | 84 |
| 46 | Sensor | FordB | 3636 | 810 | 2 | 500 |
| 47 | Image | ArrowHead | 36 | 175 | 3 | 251 |
| 48 | Image | BeetleFly | 20 | 20 | 2 | 512 |
| 49 | Image | ProximalPhalanxTW | 400 | 205 | 6 | 80 |
| 50 | Device | SmallKitchenAppliances | 375 | 375 | 3 | 720 |
| 51 | Image | FaceAll | 560 | 1690 | 14 | 131 |
| 52 | Motion | UWaveGestureLibraryX | 896 | 3582 | 8 | 315 |
| 53 | Spectrum | SemgHandSubjectCh2 | 450 | 450 | 5 | 1500 |
| 54 | Image | DistalPhalanxOutlineAgeGroup | 400 | 139 | 3 | 80 |
| 55 | Sensor | Earthquakes | 322 | 139 | 2 | 512 |
| 56 | Motion | WormsTwoClass | 181 | 77 | 2 | 900 |
| 57 | Sensor | Lightning7 | 70 | 73 | 7 | 319 |
| 58 | Spectro | Ham | 109 | 105 | 2 | 431 |
| 59 | Image | DistalPhalanxTW | 400 | 139 | 6 | 80 |
| 60 | Motion | UWaveGestureLibraryZ | 896 | 3582 | 8 | 315 |
| 61 | Device | Computers | 250 | 250 | 2 | 720 |
| 62 | Device | ElectricDevices | 8926 | 7711 | 7 | 96 |
| 63 | Motion | UWaveGestureLibraryY | 896 | 3582 | 8 | 315 |
| 64 | Sensor | InsectWingbeatSound | 220 | 1980 | 11 | 256 |
| 65 | Image | MiddlePhalanxOutlineAgeGroup | 400 | 154 | 3 | 80 |
| 66 | Image | Herring | 64 | 64 | 2 | 512 |
| 67 | Image | MiddlePhalanxTW | 399 | 154 | 6 | 80 |
| 68 | EOG | EOGVerticalSignal | 362 | 362 | 12 | 1250 |
| 69 | Sensor | DodgerLoopDay | 78 | 80 | 7 | 288 |
| 70 | Device | RefrigerationDevices | 375 | 375 | 3 | 720 |

5.2 Implementation details

The models are implemented in PyTorch and trained on a Nvidia Tesla V100 GPU using the ADAM optimizer with a Learning Rate (LR) of 0.001, a gradient clip of 0.25, and a weight decay of 0.001. We also reduce the LR by the factor of 0.1 when the validation loss stagnates for eight epochs. In the case of datasets with two classes, Binary Cross-Entropy (BCE) loss function is used, and Cross-Entropy is used for all other datasets.

5.3 Algorithmic Comparison

Table 4 compares the algorithmic performance of three ATCN families to that of InceptionTime. A comparison of Tables 4 and 2 shows that T1 has an increase in performance of 4.03% over T0 and has a reduction of $73.59 \times$ in MACs and a decrease in model size of 14.23 times over IT. In addition to reducing MACs and model sizes by 26.07 times and 4.4 times over IT, the T2 also boosts accuracy by 0.37 percent.

Table 4: Comparison of the average accuracy for seventy benchmarks from the 2018 UCR time series classification dataset

| Metric | Models | | | |
|------------------|--------|--------|--------|---------------|
| | T0 | T1 | T2 | InceptionTime |
| Average Accuracy | 83.69% | 85.73% | 86.65% | 86.28% |

In accordance with Demvsar's recommendation [32], the Friedman test is practiced and the results shows that the four classifiers are not statistically different from each other. In Fig. 8, we show the critical difference diagram of discussed classifiers. The connected classifiers by a thick line indicate that they do not have a significant difference statically at the p -value of 0.05; however, InceptionTime is undoubtedly plagued by higher computational complexity in respect to ATCN families.

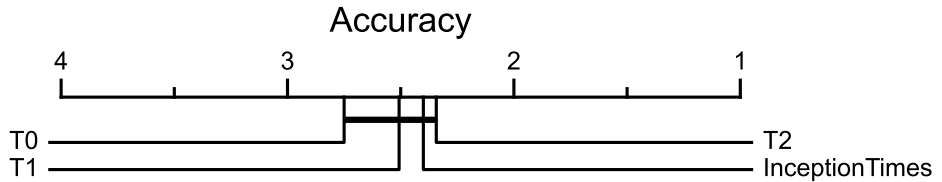


Figure 8: Critical difference diagram showing the performance of four classifier. The diagram depicts the overall average ranking of the classifiers, where those connected by a thick line show no statistically significant inconsistencies at p -value 0.05. As a result, T0, T1, T2, and InceptionTime are not significantly different.

5.4 Execution Comparison

In order to evaluate the performance of models on embedded devices, we selected STM32F746ZGT6, which has Cortex-M7 running at 216 MHz with 320 KB of RAM and 1 MB of flash memory as a microcontroller, and Cortex-A57 running at 1.43 GHz as an embedded microprocessor. We compared the execution performance and hardware utilization of all four classifiers in Table 5. The results are extracted by running model trained on *Coffee* benchmark. Compared to the T1 configuration, the T0 can reduce both RAM and flash utilization by 7.5% and 1.47%, respectively, while improving inference time by 21.42%. Due to their higher RAM requirements, T2 and InceptionTime could not be compiled. In next, we ran the all four ONNX models on A57 processor for the batch size of one. Based on the comparison between the ATCNs and InceptionTime, the ATCN families are faster by $7.49 \times$, $5.87 \times$, and $2.93 \times$, respectively.

Table 5: Resource utilization and inference time of two Cortex-M7 and Cortex-A57 platforms

| Parameters | Models | | | |
|-----------------------------|---------|---------|---------|---------------|
| | T0 | T1 | T2 | InceptionTime |
| M7 RAM utilization | 48.89% | 56.39% | - | - |
| M7 flash utilization | 14.13% | 15.89% | - | - |
| M7 inference time | 165 mS | 210 mS | - | - |
| A57 inference time | 2.81 mS | 3.58 mS | 7.16 mS | 21.05 mS |

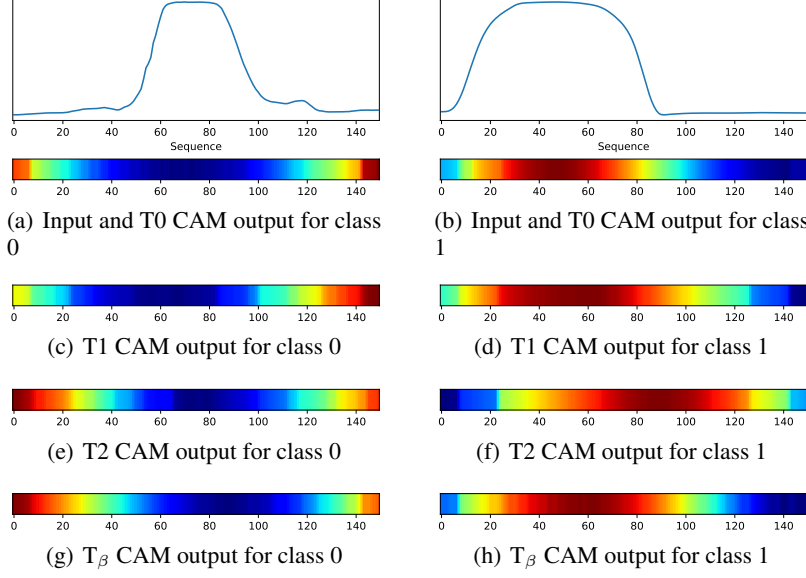


Figure 9: GunPointOldVersusYoung dataset

5.5 Architectural configuration study

During our study of the effects of kernel size, we developed a new configuration called T_β . Table 6 summarizes the T_β network configuration, FLOPs, the number of parameters, and its average accuracy. It can be seen that T_β has the same C_{out} , D , and R as T2, but the kernel size per block has been halved. Despite a greater model complexity than T1, both FLOPs and model size, the results show that T1 is still more accurate than T_β . As an aid to understanding this behavior, we depict the inputs and Class Activation Mapping (CAM) of two benchmarks in Fig. 9 and Fig. 10. When the model correctly classified the input signal, CAMs are calculated by multiplying the input of global average pooling by the weight matrices of the correct class index.

The activation heatmaps for class 0, shown in Fig. 9, have the lowest value around the input signal magnitude. Consequently, for class 0, the probability of output approaches zero. However, we can observe the activation heatmaps for class 1 have the highest value around the signal magnitude, which leads to the output probability being one. For multiclass classification problems depicted in Fig. 10, we can see models activate based on the perceived nuances of signal shapes. For instance, the T0 model, Fig. 10(a) ~ Fig. 10(a), classifies the input as class 0 based on the form observed in sequence ~ 10 to ~ 80 , as class 1 based on unique transition observed in the middle of the sequence, and as class 2 based on the curve recognized in ~ 70 to ~ 150 . In respect to T_β , this model shows a coarse-grained transition, note sequence ~ 20 to ~ 60 in Fig. 9(h) and ~ 150 to ~ 240 in Fig. 10(j). This indicates that T_β has a lower receptive field compared to T1 and T2, both of which have the same kernel size. As a result of the higher receptive field of T1, the model is able to predict the classes more precisely, although it has less model complexity in both forms of FLOPs and the number of parameters.

Table 6: Model configuration and accuracy performance of T_β

| Model | Parameters | | | | | | |
|-----------|----------------------------------|--------------------------|-----------------------------|--|-----------|---------|------------------|
| | C_{out} | D | K | R | FLOPs | Params# | Average Accuracy |
| T_β | [64, 32, 32, 16, 16, 32, 32, 64] | [1, 2, 2, 4, 4, 6, 6, 8] | [32, 16, 16, 8, 8, 4, 4, 2] | [$\frac{1}{2}$, 1, 1, 1, 1, 1, 1, 1] | 7,303,136 | 86,240 | 84.94% |

6 Conclusion

ATCN is proposed here for lightweight real-time processing of time-series on embedded and edge devices. In order to reduce the number of MAC operations and model size, we introduced STCB as a main computational block. STCB blocks are able to be sequenced in a variety of configurations to build scalable ATCNs. We also presented a framework, called *ATCN Model Synthesizer*, to build different ATCN models. The result of *ATCN Model Synthesizer* is a family of compact networks with formalized hyper-parameters that allow the model architecture to be configurable and adjusted

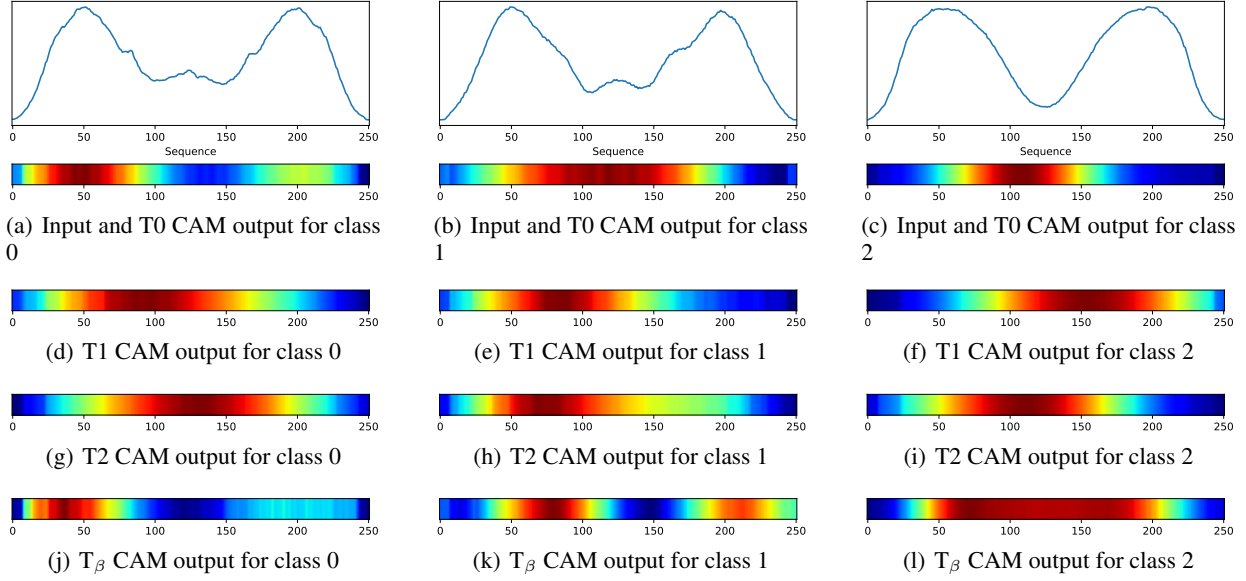


Figure 10: ArrowHead dataset

based on the application requirements. Through the use of model synthesizer and ATCN reconfigurability, we have developed three agile models, T0, T1, and T2, two of which can be executed on ARM Cortex-M7 microcontrollers. The experimental results over 2018 UCR time classification benchmarks indicate that the T0 configuration can reduce the MACs and model size by $102.38\times$ and $16.84\times$ over InceptionTime, respectively. T1 performance is 4.03% better than T0 and has a $73.59\times$ reduction in MACs, and a $14.23\times$ reduction in model size over InceptionTime. Both T0 and T1 can be executed on an ARM Cortex-M7 microcontroller explained in the experimental section in detail. As a final improvement, T3 reduces the MACs and model size for $26.07\times$ and $4.4\times$ over IT while increasing accuracy by 0.37% .

References

- [1] C. Neff, M. Mendieta, S. Mohan, M. Baharani, S. Rogers, and H. Tabkhi, “Revamp2t: Real-time edge video analytics for multicamera privacy-aware pedestrian tracking,” *IEEE Internet of Things Journal*, vol. 7, no. 4, pp. 2591–2602, 2020.
- [2] B. Blanco-Filgueira, D. García-Lesta, M. Fernández-Sanjurjo, V. M. Brea, and P. López, “Deep learning-based multiple object visual tracking on embedded system for iot and mobile edge computing applications,” *IEEE Internet of Things Journal*, vol. 6, no. 3, pp. 5423–5431, 2019.
- [3] M. Xu, M. Gao, Y. Chen, L. Davis, and D. Crandall, “Temporal recurrent networks for online action detection,” in *2019 IEEE/CVF International Conference on Computer Vision (ICCV)*, 2019, pp. 5531–5540.
- [4] G. Chen, C. Zhang, and Y. Zou, “Afnet: Temporal locality-aware network with dual structure for accurate and fast action detection,” *IEEE Transactions on Multimedia*, pp. 1–1, 2020.
- [5] S. D. Goodfellow, A. Goodwin, R. Greer, P. C. Laussen, M. Mazwi, and D. Eytan, “Towards understanding ecg rhythm classification using convolutional neural networks and attention mappings,” ser. Proceedings of Machine Learning Research, F. Doshi-Velez, J. Fackler, K. Jung, D. Kale, R. Ranganath, B. Wallace, and J. Wiens, Eds., vol. 85. Palo Alto, California: PMLR, 17–18 Aug 2018, pp. 83–101. [Online]. Available: <http://proceedings.mlr.press/v85/goodfellow18a.html>
- [6] S. Saadatnejad, M. Oveis, and M. Hashemi, “Lstm-based ecg classification for continuous monitoring on personal wearable devices,” *IEEE Journal of Biomedical and Health Informatics*, vol. 24, no. 2, pp. 515–523, 2020.
- [7] Y. Li, Z. Xia, and Y. Zhang, “Standalone systolic profile detection of non-contact scg signal with lstm network,” *IEEE Sensors Journal*, vol. 20, no. 6, pp. 3123–3131, 2020.

[8] M. Baharani, M. Biglarbegian, B. Parkhideh, and H. Tabkhi, “Real-time deep learning at the edge for scalable reliability modeling of si-mosfet power electronics converters,” *IEEE Internet of Things Journal*, vol. 6, no. 5, pp. 7375–7385, 2019.

[9] M. Biglarbegian, M. Baharani, N. Kim, H. Tabkhi, and B. Parkhideh, “Scalable reliability monitoring of gan power converter through recurrent neural networks,” in *2018 IEEE Energy Conversion Congress and Exposition (ECCE)*, 2018, pp. 7271–7277.

[10] Y. Zhang, R. Xiong, H. He, and M. G. Pecht, “Long short-term memory recurrent neural network for remaining useful life prediction of lithium-ion batteries,” *IEEE Transactions on Vehicular Technology*, vol. 67, no. 7, pp. 5695–5705, 2018.

[11] B. Zhang, D. Xiong, J. Xie, and J. Su, “Neural machine translation with gru-gated attention model,” *IEEE Transactions on Neural Networks and Learning Systems*, pp. 1–11, 2020.

[12] Q. Li, X. Zhang, J. Xiong, W.-m. Hwu, and D. Chen, “Implementing neural machine translation with bi-directional gru and attention mechanism on fpgas using hls,” in *Proceedings of the 24th Asia and South Pacific Design Automation Conference*, ser. ASPDAC ’19. New York, NY, USA: Association for Computing Machinery, 2019, p. 693–698. [Online]. Available: <https://doi.org/10.1145/3287624.3287717>

[13] S. Hochreiter and J. Schmidhuber, “Long short-term memory,” *Neural Comput.*, vol. 9, no. 8, p. 1735–1780, Nov. 1997. [Online]. Available: <https://doi.org/10.1162/neco.1997.9.8.1735>

[14] J. Chung, C. Gulcehre, K. Cho, and Y. Bengio, “Empirical evaluation of gated recurrent neural networks on sequence modeling,” 2014.

[15] S. Bai, J. Z. Kolter, and V. Koltun, “An empirical evaluation of generic convolutional and recurrent networks for sequence modeling,” *CoRR*, vol. abs/1803.01271, 2018. [Online]. Available: <http://arxiv.org/abs/1803.01271>

[16] A. van den Oord, S. Dieleman, H. Zen, K. Simonyan, O. Vinyals, A. Graves, N. Kalchbrenner, A. W. Senior, and K. Kavukcuoglu, “Wavenet: A generative model for raw audio,” *CoRR*, vol. abs/1609.03499, 2016. [Online]. Available: <http://arxiv.org/abs/1609.03499>

[17] A. Waibel, T. Hanazawa, G. Hinton, K. Shikano, and K. J. Lang, “Phoneme recognition using time-delay neural networks,” *IEEE Transactions on Acoustics, Speech, and Signal Processing*, vol. 37, no. 3, pp. 328–339, 1989.

[18] S. Bai, J. Z. Kolter, and V. Koltun, “An empirical evaluation of generic convolutional and recurrent networks for sequence modeling,” 2018.

[19] H. Ismail Fawaz, B. Lucas, G. Forestier, C. Pelletier, D. F. Schmidt, J. Weber, G. I. Webb, L. Idoumghar, P.-A. Muller, and F. Petitjean, “Inceptiontime: Finding alexnet for time series classification,” *Data Mining and Knowledge Discovery*, vol. 34, no. 6, pp. 1936–1962, Nov 2020. [Online]. Available: <https://doi.org/10.1007/s10618-020-00710-y>

[20] H. A. Dau, A. Bagnall, K. Kamgar, C.-C. M. Yeh, Y. Zhu, S. Gharghabi, C. A. Ratanamahatana, and E. Keogh, “The ucr time series classification archive,” October 2018, https://www.cs.ucr.edu/~eamonn/time_series_data_2018/.

[21] A. van den Oord, S. Dieleman, H. Zen, K. Simonyan, O. Vinyals, A. Graves, N. Kalchbrenner, A. W. Senior, and K. Kavukcuoglu, “Wavenet: A generative model for raw audio,” *ArXiv*, vol. abs/1609.03499, 2016.

[22] C. Lea, M. D. Flynn, R. Vidal, A. Reiter, and G. D. Hager, “Temporal convolutional networks for action segmentation and detection,” in *2017 IEEE Conference on Computer Vision and Pattern Recognition (CVPR)*, 2017, pp. 1003–1012.

[23] J. Gehring, M. Auli, D. Grangier, D. Yarats, and Y. N. Dauphin, “Convolutional sequence to sequence learning,” *CoRR*, vol. abs/1705.03122, 2017. [Online]. Available: <http://arxiv.org/abs/1705.03122>

[24] A. Pandey and D. Wang, “Tcnn: Temporal convolutional neural network for real-time speech enhancement in the time domain,” in *ICASSP 2019 - 2019 IEEE International Conference on Acoustics, Speech and Signal Processing (ICASSP)*, 2019, pp. 6875–6879.

[25] R. Sen, H.-F. Yu, and I. S. Dhillon, “Think globally, act locally: A deep neural network approach to high-dimensional time series forecasting,” in *Advances in Neural Information Processing Systems*, 2019, pp. 4837–4846.

[26] C. Szegedy, S. Ioffe, V. Vanhoucke, and A. A. Alemi, “Inception-v4, inception-resnet and the impact of residual connections on learning,” in *Proceedings of the Thirty-First AAAI Conference on Artificial Intelligence*, ser. AAAI’17. AAAI Press, 2017, p. 4278–4284.

- [27] J. Lines, S. Taylor, and A. Bagnall, “Hive-cote: The hierarchical vote collective of transformation-based ensembles for time series classification,” in *2016 IEEE 16th International Conference on Data Mining (ICDM)*, 2016, pp. 1041–1046.
- [28] M. Carreras, G. Deriu, L. Raffo, L. Benini, and P. Meloni, “Optimizing temporal convolutional network inference on fpga-based accelerators,” *IEEE Journal on Emerging and Selected Topics in Circuits and Systems*, pp. 1–1, 2020.
- [29] K. He, X. Zhang, S. Ren, and J. Sun, “Deep residual learning for image recognition,” in *2016 IEEE Conference on Computer Vision and Pattern Recognition (CVPR)*, June 2016, pp. 770–778.
- [30] T. T. Um, F. M. J. Pfister, D. Pichler, S. Endo, M. Lang, S. Hirche, U. Fietzek, and D. Kulic, “Data augmentation of wearable sensor data for parkinson’s disease monitoring using convolutional neural networks,” in *Proceedings of the 19th ACM International Conference on Multimodal Interaction*, ser. ICMI ’17. New York, NY, USA: Association for Computing Machinery, 2017, p. 216–220. [Online]. Available: <https://doi.org/10.1145/3136755.3136817>
- [31] A. Le Guennec, S. Malinowski, and R. Tavenard, “Data augmentation for time series classification using convolutional neural networks,” in *ECML/PKDD workshop on advanced analytics and learning on temporal data*, 2016.
- [32] J. Demšar, “Statistical comparisons of classifiers over multiple data sets,” *The Journal of Machine Learning Research*, vol. 7, pp. 1–30, 2006.